Chemical Engineering Journal 520 (2025) 165892

Contents lists available at ScienceDirect

Chemical Engineering Journal

journal homepage: www.elsevier.com/locate/cej

Molecular engineering and synergistic redox-active hexaazatrinaphthalene and pyrene-based conjugated microporous polymers for superior faradaic supercapacitor energy storage

Mohamed Gamal Mohamed [a,b,*,1], Bhargabi Halder [c,1], Poonam Nagendra Singh [a], Ahmed A.K. Mohammed [b], Perumal Elumalai [c,**], Shiao-Wei Kuo [a,d,*]

[a] Department of Materials and Optoelectronic Science, Center for Functional Polymers and Supramolecular Materials, National Sun Yat-Sen University, Kaohsiung 804, Taiwan
[b] Department of Chemistry, Faculty of Science, Assiut University, Assiut 71515, Egypt
[c] Electrochemical Energy Storage Lab, Department of Green Energy Technology, Madanjeet School of Green Energy Technologies, Pondicherry University, Puducherry 605014, India
[d] Department of Medicinal and Applied Chemistry, Kaohsiung Medical University, Kaohsiung 807, Taiwan

ARTICLE INFO

Keywords:
Pyrene
Redox-active hexaazatrinaphthalene
Conjugated microporous polymers
Supercapacitor
Faradaic behavior

ABSTRACT

Conjugated microporous polymers (CMPs) have arisen as a rapidly progressing category of materials, demonstrating immense potential across various technological domains, particularly in energy storage. In this study, we strategically synthesized two distinct CMP variants PyPH-HATN CMP-0.75 and PyPH-HATN CMP-1.5 via the Suzuki coupling reaction, modulating the monomeric ratio of 1,3,6,8-tetrabromopyrene (Py-4Br) and 2,8,14-tribromodiquinoxalino[2,3-a:2′,3′-c]phenazine (HATN-3Br) in the presence of 1,4-phenylenediboronic acid [PH-$(B(OH)_2)_2$] to engineer high-performance supercapacitor (SC) electrodes. The structural integrity and physicochemical properties of PyPH-HATN CMP-0.75 and PyPH-HATN CMP-1.5 were comprehensively analyzed through multiple advanced techniques. Notably, PyPH-HATN-CMP-1.5 exhibited a well-defined rod-like morphology, demonstrating the efficacy of monomeric tuning in tailoring the polymer architecture. Electrochemical evaluations underscored the superior capacitive behavior of the PyPH-HATN CMP-1.5 electrode, delivering an exceptional specific capacitance of 1790 $F.g^{-1}$ at a 1 $A.g^{-1}$. The charge storage mechanism was characterized by a dominant diffusive contribution (75 %) complemented by a capacitive component (25 %) at 1 $mV.s^{-1}$. Furthermore, the PyPH-HATN CMP-1.5 electrode showed remarkable rate capability and outstanding cycling stability (97 %) of its initial capacitance after 5000 charge-discharge cycles at 20 $A.g^{-1}$. These results unequivocally highlight the potential of these architecturally engineered PyPH-HATN CMP-1.5 electrodes as next-generation organic electrode materials for high-performance supercapacitors (SCs), paving the way for their integration into advanced energy storage systems.

1. Introduction

The rapid surge in industrialization and the extensive reliance on fossil fuels have significantly contributed to pressing global challenges, including environmental degradation, resource depletion, and climate change [1–4]. The unsustainable consumption of natural resources, coupled with escalating energy needs, has underscored the urgent need to develop efficient and sustainable energy storage solutions [5–9]. Among the wide range of energy storage technologies, electrochemical devices, notably batteries and supercapacitors (SCs) are regarded as the

* Corresponding authors. M.G. Mohamed and S.W. Kuo, Department of Materials and Optoelectronic Science, Center for Functional Polymers and Supramolecular Materials, National Sun Yat-Sen University, Kaohsiung 804, Taiwan.
** Correspondence to: P. Elumalai, Electrochemical Energy Storage Lab, Department of Green Energy Technology, Madanjeet School of Green Energy Technologies, Pondicherry University, Puducherry 605014, India.
E-mail addresses: mgamal.eldin12@yahoo.com, mgamal.eldin12@aun.edu.eg (M.G. Mohamed), drperumalelumalai@pondiuni.ac.in (P. Elumalai), kuosw@faculty.nsysu.edu.tw (S.-W. Kuo).
[1] These authors contributed equally.

https://doi.org/10.1016/j.cej.2025.165892
Received 2 March 2025; Received in revised form 2 July 2025; Accepted 10 July 2025
Available online 10 July 2025

most efficient solutions. While batteries function as energy-storage devices, supercapacitors are designed for high-power applications, making them indispensable in rapid energy delivery scenarios. SCs not only regulate surge power but also exhibit remarkable advantages such as superior charge-discharge rates, exceptional cycling stability, and environmental sustainability [10–13]. Owing to these attributes, SCs hold immense potential for deployment in diverse applications, including wind turbines, electric vehicles, biomedical defibrillators, memory backup systems, and other advanced technologies [10–14]. Based on their charge storage mechanisms, SCs are commonly classified into two main types: electric double-layer capacitors (EDLCs) and pseudocapacitors [15–18]. EDLCs retain electrical energy by reversibly adsorbing and desorbing electrolyte ions on the electrode surface, relying on electrostatic interactions without any charge transfer [15–18]. In contrast, pseudocapacitors operate via an electrochemical mechanism in which charge transfer occurs through redox reactions at the electrode interface [15–18]. When EDLC and pseudocapacitive behaviors coexist within a system, both Faradaic and non-Faradaic processes contribute synergistically to charge storage, thereby enhancing the overall capacitance and electrochemical stability [19–25].

The significance of conjugated microporous polymers (CMPs) matrices is rapidly expanding across a spectrum of applications, particularly in energy storage, gas sorption, and catalysis [26–31]. Conjugated microporous polymers (CMPs), characterized by their π-conjugated network and microporous architecture, have emerged as a promising class of materials for advanced supercapacitor (SC) electrodes [30–32]. Their unique combination of ultralow density, high surface area, exceptional pore volume, and excellent thermal stability provides a favorable platform for efficient ion transport and electrolyte accessibility—key factors in optimizing SC performance [30–32]. The integration of redox-active π-conjugated units within their framework further enhances charge storage through faradaic processes, contributing to improved specific capacitance and cycling stability [33–36]. Unlike conventional polymers, CMPs possess intrinsic porosity and electrical conductivity, making them ideal candidates for high-performance SC electrode materials that demand both rapid charge transfer and robust structural integrity [37–41]. Owing to the vast selection of monomeric precursors and synthetic routes, conjugated microporous polymers (CMPs) offer exceptional tunability, enabling precise control over their structure, porosity, and electrochemical functionality. This structural versatility is especially advantageous for SC electrodes, where optimizing pore architecture and surface chemistry is critical for maximizing ion diffusion, charge storage, and conductivity. By tailoring the molecular design, CMPs can be engineered to achieve enhanced electrochemical performance, making them highly attractive as next-generation electrode materials for high-efficiency SCs. Various synthetic strategies have been employed to fabricate CMPs, encompassing oxidative polymerization and conventional cross-coupling protocols such as Suzuki-Miyaura, Sonogashira-Hagihara, and Yamamoto coupling. These methodologies have enabled the development of CMPs with diverse architectures and finely tuned functionalities, further advancing their potential in next-generation energy storage technologies [30,31,42].

The pyrene (Py) moiety, characterized by its extended π-conjugation and intrinsically planar architecture, exhibits potent electron-donating properties [43,44]. Py plays a pivotal role in π-conjugated organic semiconductors, which modulates molecular stacking interactions and augments charge transport efficiency [45–48]. In the realm of energy storage, pyrene-based CMPs have demonstrated remarkable electrochemical performance. For instance, Zhao et al. demonstrated the fabrication of porous carbon from a pyrene-based CMP, achieving a capacitance of 301 $F.g^{-1}$, measured at 1 $A.g^{-1}$ [49]. Similarly, Singh et al. synthesized ultrastable CMPs incorporating Py units with a specific capacitance of 300 $F.g^{-1}$ at 0.5 $A.g^{-1}$ [50]. 1,4,5,8,9,12-Hexaazatriphenylene (HATN), also referred to as [2,3-f:2′,3′-h]dipyrazinoquinoxaline, is a rigid, planar, and electron-deficient discotic aromatic molecule renowned for its superior π–π stacking capabilities [51,52]. As a nitrogen-rich polyheterocyclic system with an extended conjugated framework, HATN possesses outstanding electronic and structural characteristics, making it a fundamental molecular platform for the strategic design of advanced functional materials for SCs [51–54]. The inherent structural robustness of these materials enables finely tuned electronic modulation via strategic heteroatom doping, particularly nitrogen (N), which significantly augments transport pathways and enhances overall electrochemical behavior [55,56]. Moreover, the deliberate integration of donor (PyPH)–acceptor (HATN) motifs into the conjugated microporous polymer (CMP) frameworks facilitates effective bandgap engineering and lowers redox potentials, driven by pronounced intramolecular charge-transfer interactions [57]. Collectively, these synergistic effects yield superior charge carrier mobility and elevated power densities, underscoring their potential as advanced materials for high-performance electrochemical systems [58,59].

The polycondensation coupling process, specifically the Suzuki cross-coupling reaction, was employed to synthesize two redox-active CMP samples, denoted as PyPH-HATN CMP-0.75 and PyPH-HATN CMP-1.5 using Py-4Br and HATN-3Br in the presence of PH-$(B(OH)_2)_2$ as a linker as the fundamental monomeric building blocks for high-performance SCs applications. The structural, morphological, and physicochemical characteristics of the resulting CMPs were meticulously elucidated through an array of advanced spectroscopic and microscopic analytical techniques. The incorporation of the redox-active HATN unit endows these CMPs with exceptional electrochemical properties, positioning them as highly promising precursors for SC electrodes. Galvanostatic charge-discharge (GCD) and cyclic voltammetry (CV) assessments revealed that PyPH-HATN CMP-1.5 exhibits outstanding specific capacitance values along with remarkable cyclic stability, surpassing conventional CMP-based SCs. These findings underscore the pivotal role of rationally designed HATN-anchored CMPs in advancing sustainable energy technologies. Beyond their application in supercapacitors, the intrinsic structural tunability and superior electrochemical performance of these materials render them compelling candidates for multi-functional clean energy applications.

2. Experimental section

2.1. Materials

From Across and Sigma–Aldrich, pyrene (Py), 4-bromobenzene-1,2-diamine [4-Br-BZ-$2NH_2$], nitrobenzene (BZ-NO_2), bromine solution (Br_2), $Pd(PPh_3)_4$, glacial acetic acid (AcOH), cyclohexanone octahydrate, potassium carbonate (K_2CO_3), 1,4-phenylenediboronic acid PH-$(B(OH)_2)_2$, and anhydrous magnesium sulfate ($MgSO_4$) were obtained.

2.2. Synthesis of Py-4Br [59]

Py (0.85 g, 4.3 mmol) in BZ-NO_2 (50 mL) and Br_2 (1 mL, 19.43 mmol) were added with stirring at 130–140 °C for 24 h. Then, the product was filtered and washed several times with EtOH to remove BZ-NO_2 and excess Br_2 to acquire Py-4Br as a pale-light solid. FTIR (Fig. S1): aromatic C—H (3078 cm^{-1}), 1591, 1462 cm^{-1} (C=C) and C—Br (671 cm^{-1}). HR ES-MS (*m/z*): calcd for ($C_{16}H_6Br_4$), 517.87; found, 517.7148 [Fig. S2].

2.3. Synthesis of HATN-3Br

A solution of 4-Br-BZ-$2NH_2$ (3 g, 16.04 mmol) in 150 mL of AcOH under continuous stirring. Subsequently, cyclohexanone octahydrate (1.7 g, 5.35 mmol) was introduced into the reaction mixture and kept at the refluxing temperature of 120 °C for 24 h under a nitrogen atmosphere with constant agitation. The crude product was isolated via vacuum filtration and subjected to sequential purification through extensive washing with deionized H_2O, EtOH, and hot AcOH. The

resulting yellow-green powder was then subjected to oxidative treatment by stirring in 50 mL of 35 wt% HNO_3 at 120 °C. The final material was acquired as a green solid, designated as HATN-3Br. FTIR (Fig. S3): aromatic C—H (3068 cm^{-1}), C═N (1615 cm^{-1}), 1516, 1481 cm^{-1} (C=C). HR ES-MS (*m/z*): calcd for ($C_{24}H_9Br_3N_6$), 621.09; found, 621.8403 [Fig. S4].

2.4. Synthesis of PyPH-HATN CMP-0.75 and PyPH-HATN CMP-1.5

To prepare PyPH-HATN CMP-0.75: In a Schlenk flask, Py-4Br (0.3 g, 0.57 mmol), HATN-3Br (0.27 g, 0.44 mmol), PH-$(B(OH)_2)_2$ (0.24 g, 1.45 mmol), K_2CO_3 (2 M, 10 mL), and $Ph(PPh_3)_4$ (0.065 mmol) were prepared. To this mixture, 20 mL of water and 40 mL of DMF were added, and the temperature of the reaction mixture at 140 °C with constant stirring for three days. The same method was used the same to prepare PyPH-HATN CMP-1.5 by Py-4Br (0.3 g, 0.57 mmol), HATN-3Br (0.54 g, 0.88 mmol), PH-$(B(OH)_2)_2$ (0.3 g, 1.74 mmol). The resulting green precipitates of PyPH-HATN CMP-0.75 [Scheme S1] and PyPH-HATN CMP-1.5 [Scheme S2] were washed with various organic solvents to remove unreacted materials and impurities.

3. Results and discussions

3.1. Synthesis and characterization of PyPH-HATN CMP-0.75 and PyPH-HATN CMP-1.5

The synthesis of key building precursors, Py-4Br and HATN-3Br, was carried out following the schematic approach illustrated in Fig. 1. Py-4Br was obtained in high yield through the bromination of Py using Br_2 in the presence of BZ-NO_2 at an elevated temperature of 130–140 °C [Fig. 1(a)]. The HATN-3Br was synthesized with superior purity and outstanding yield through the reaction of 4-Br-BZ-2NH_2 with cyclohexanone octahydrate at 120 °C, employing AcOH as both solvent and catalyst, resulting in a green solid [Fig. 1(b)]. The successful formation of HATN-3Br was confirmed using FT-IR spectroscopy, which demonstrated the complete disappearance of FTIR absorption bands related to C═O and NH_2 groups. Additionally, new peaks emerged at 3068, 1615, 1516, and 1481 cm^{-1}, corresponding to C—H in the phenyl rings, C═N, C—N, and C═C bonds, respectively, in the HATN moiety [Fig. S1]. As illustrated in Fig. 1(c), the organic electrodes, PyPH-HATN CMP-0.75 and PyPH-HATN CMP-1.5, designed for SCs applications, were synthesized through the Suzuki reaction of Py-4Br with HATN-3Br in the presence of PH-$(B(OH)_2)_2$ as a linker agent. These green powder materials incorporate the highly active HATN moiety, rich in redox-active functional groups, thereby enhancing their electrochemical performance [54,60,61]. The functional groups present in PyPH-HATN CMP-0.75 and PyPH-HATN CMP-1.5 were confirmed through FT-IR spectroscopy at 25 °C, as depicted in Fig. 2(a). The spectra of both PyPH-HATN CMP-0.75 and PyPH-HATN CMP-1.5 exhibited strong and nearly identical absorption peaks. Notably, distinct peaks in the range 3047–3051 cm^{-1} and 1613–1603 cm^{-1} regions relate to the aromatic C—H stretching and C═N, respectively [54]. The characteristic absorption at 1613–1604 cm^{-1} is for C═C units [54]. The carbon frameworks of PyPH-HATN CMP-0.75 and PyPH-HATN CMP-1.5 were further characterized by solid-state ^{13}C NMR (SSNMR) spectroscopy. Distinct peaks were observed in the ^{13}C SSNMR spectra at 142.56–118.87 ppm and 143.54 ppm, corresponding to aromatic carbon signals from the PyPH and HATN moieties, respectively. An additional peak at 153.93 ppm is attributed to the C=N units, as shown in Fig. S5. The chemical composition of PyPH-HATN CMP-1.5, as determined by X-ray photoelectron spectroscopy (XPS), confirmed the existence of a substantial amount of carbon (C) and nitrogen (N) atoms, as illustrated in the survey

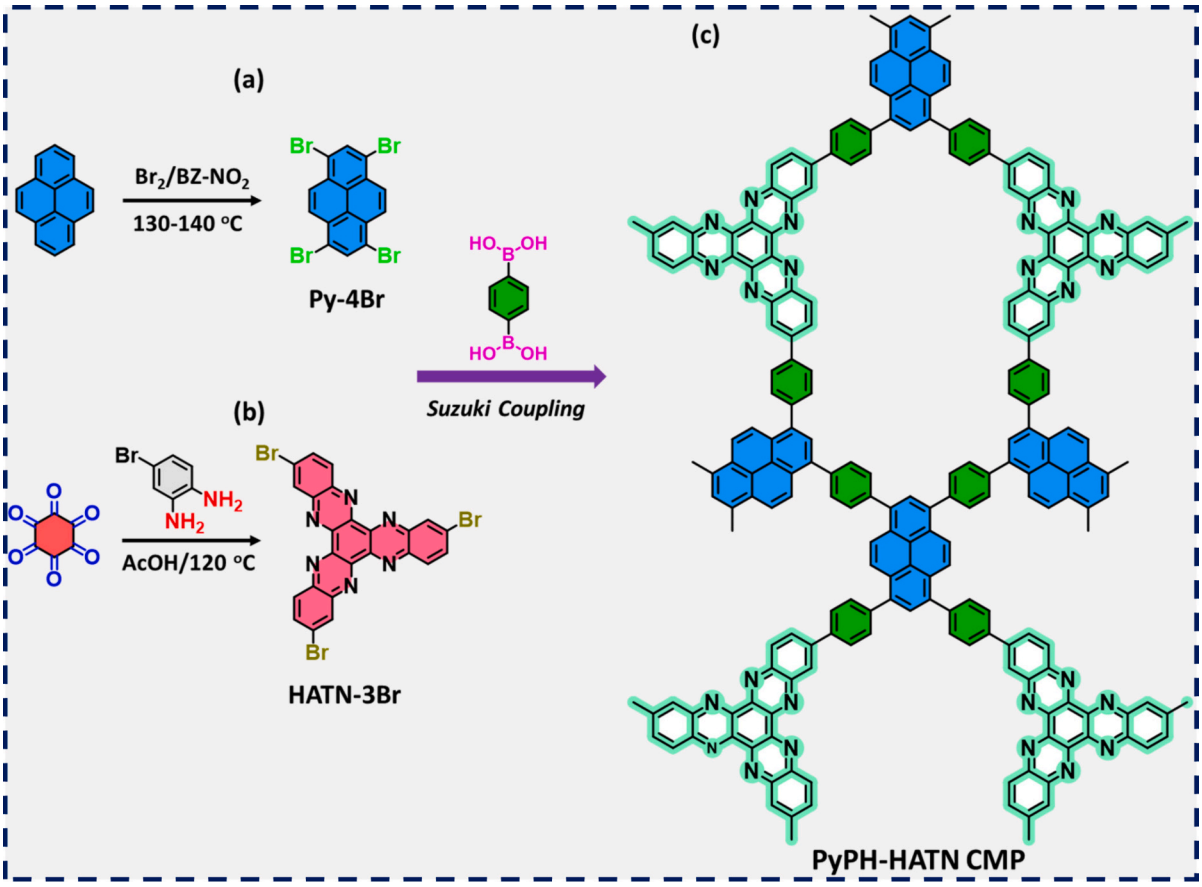

Fig. 1. Schematic for the preparation of the (a) Py-4Br, (b) HATN-3Br, and (c) PyPH-HATN CMP [PyPH-HATN CMP-0.75 and PyPH-HATN CMP-1.5].

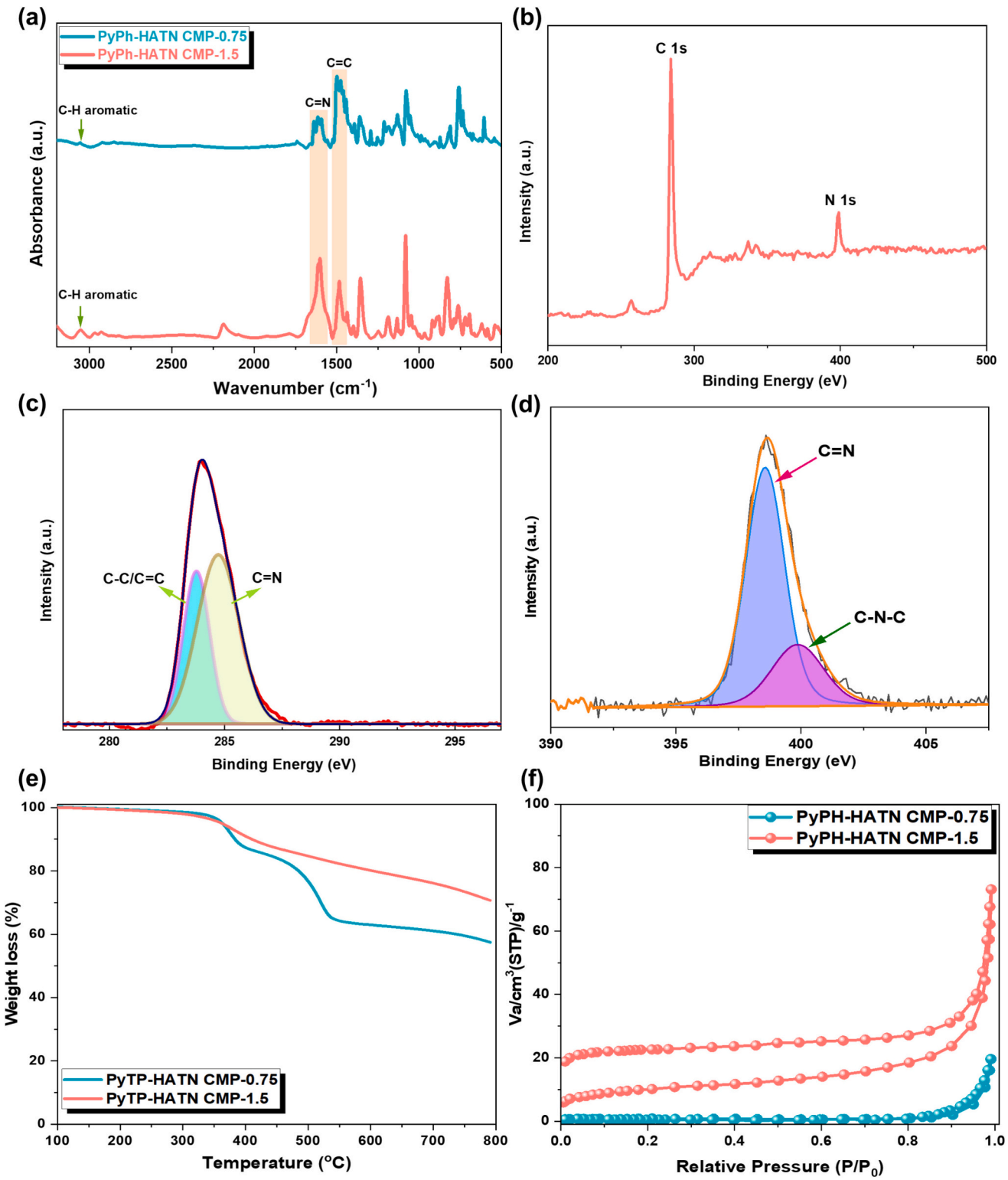

Fig. 2. (a) FTIR profiles recorded for the PyPH-HATN CMP-0.75 and PyPH-HATN CMP-1.5. (b) XPS survey spectrum of PyPH-HATN CMP-1.5, (c, d) Deconvolution spectra of the C 1 s and N 1 s in the PyPH-HATN CMP-1.5 framework. (e) TGA traces and (f) N_2 adsorption-desorption isotherms of the PyPH-HATN CMP-0.75 and PyPH-HATN CMP-1.5.

spectrum [Fig. 2(b)]. Deconvolution of the C 1s spectrum revealed two distinct peaks at 285.2 eV and 284.0 eV, corresponding to C═N and C–C/C=C bonds, respectively [Fig. 2(c)] [54].

Additionally, the deconvoluted peaks of N 1s at 398.5 and 399.8 eV in Fig. 2(d) are severally assignable to C═N bond and C-N-C linkage within the HATN unit. The incorporation of nitrogen heteroatoms significantly enhances electrochemical performance by facilitating pseudocapacitance, thereby increasing the overall capacitance when the material is immersed in an electrolyte solution [54,60]. The thermal stability of PyPH-HATN CMP-0.75 and PyPH-HATN CMP-1.5 was assessed using thermogravimetric analysis (TGA), as shown in Fig. 2(e). Both materials demonstrated excellent thermal resistance, attributed to

the robust Py and HATN unit linkage formed and the formation of a rigid aromatic skeleton via the Suzuki coupling reaction. Specifically, PyPH-HATN CMP-1.5 exhibited a higher char yield (71 wt% and T_{d10} = 410 °C) than that of PyPH-HATN CMP-0.75 (58 wt% and T_{d10} = 383 °C) under a N_2 atmosphere at 800 °C [60,62]. Powder X-ray diffraction (PXRD) analysis revealed structural differences between the two materials. PyPH-HATN CMP-0.75 and PyPH-HATN CMP-1.5 exhibited broad diffraction peaks, indicating an amorphous nature as presented in Fig. S6. The Brunauer–Emmett–Teller (BET) method was employed to determine the specific surface areas of PyPH-HATN CMP-0.75 and PyPH-HATN CMP-1.5. The adsorption-desorption isotherms, presented in Fig. 2(f), revealed distinct textural characteristics. PyPH-HATN CMP-1.5 followed a Type-IV isotherm, characteristic of meso- and microporous structures. Whereas PyPH-HATN CMP-0.75 exhibited a Type-III isotherm, indicative of nonporous or weakly porous materials. The calculated surface areas (S_{BET}) of PyPH-HATN CMP-0.75 and PyPH-HATN CMP-1.5 were determined to be 15 and 55 $m^2.g^{-1}$, respectively. According to the nonlocal density functional theory (NLDFT) method, the pore diameters of PyPH-HATN CMP-1.5 are primarily distributed between 1.75 and 9.4 nm, as shown in Fig. S7. The morphological features of PyPH-HATN CMP-0.75 and PyPH-HATN CMP-1.5 were examined using a high-resolution scanning electron microscope (SEM) and SEM-EDS analyses as presented in Fig. 3. The SEM images of the PyPH-HATN CMP-0.75 revealed the formation of aggregated nanoparticles that were evenly dispersed across the material's surface [Fig. 3 (a-d)], while PyPH-HATN CMP-1.5 displayed an assembly of rod-like structures with well-defined pores and sharp edges [Fig. 3(e-h)]. The distinct morphologies observed for PyPH-HATN CMP-0.75 and PyPH-HATN CMP-1.5, as evidenced by SEM imaging, arise from differences in HATN feed ratios. At lower HATN feed ratios (e.g., PyPH-HATN CMP-0.75), the polymerization process lacks structural precision, resulting in randomly cross-linked, amorphous networks with pronounced particle agglomeration. In contrast, increasing the HATN content (e.g., PyPH-HATN CMP-1.5) enhances the density of reactive sites and extends π-conjugation, thereby directing the formation of more ordered, anisotropic architectures characterized by rod-like morphologies. This morphological evolution is further driven by intensified π–π stacking interactions that promote self-assembly, underscoring the synergistic influence of both kinetic and thermodynamic factors modulated by the HATN feed ratio. The SEM-EDS analysis confirmed the elemental composition of PyPH-HATN CMP-1.5, revealing a predominant homogeneous dispersion of C and N atoms throughout PyPH-HATN CMP-1.5 frameworks [Fig. S8]. TEM analysis further confirmed the porous nature of both PyPH-HATN CMP-0.75 and PyPH-HATN CMP-1.5, with no discernible lattice fringes, indicating their weakly crystalline structures [Fig. S9].

3.2. Electrochemical activity of PyPH-HATN CMP-0.75 and PyPH-HATN CMP-1.5 electrodes

A three-electrode setup was constructed in order to assess the performance of the PyPH-HATN CMP-0.75 and PyPH-HATN CMP-1.5 electrodes. On the constructed three-electrode cell, the GCD profiles were recorded at several current rates, and the CV profiles were noted at a voltage ranging from 0 to −1 V at various scan rates. In a three-electrode cell setup with an aqueous 1 M KOH electrolyte, the charge storage characteristics of the PyPH-HATN CMP-0.75 and PyPH-HATN CMP-1.5 electrodes were investigated. The CV profiles were performed on the three-electrode cell at several scan rates of 5 to 200 $mV.s^{-1}$ in the above-mentioned voltage. The acquired CV profiles are displayed in Fig. 4(a) and (b). A symmetrical redox peaks CV profile with prominent redox peaks at −0.7 V is produced at all scan rates, indicating a Faradaic process as the dominant mode for charge storage [54,63–65]. The current response in the CV profiles with ascending scan rate indicates that the organic electrode materials have a significant rate capability, which is a useful property for building a supercapacitor. Given the size of the area under the CV curves, the PyPH-HATN CMP-0.75 and PyPH-HATN CMP-1.5 electrodes appear to retain charge effectively. Compared to the PyPH-HATN CMP-0.75 electrode, where capacitive behavior appears more prominent, the CV profile of the PyPH-HATN CMP-1.5 electrode exhibits sharper redox peaks that contribute to a strong Faradaic reaction. The redox peaks observed in the CV profiles could be attributed to the reversible redox transitions involving the nitrogen atoms within the HATN core in PyPH-HATN CMP. Specifically, these correspond to the reversible n-type redox processes of the electron-deficient heterocyclic units (C=N/C–N–K), which undergo potassium-coupled electron transfer (PCET) in the presence of the aqueous electrolyte. General redox process:

$$C = N + K^+ + e^- \rightleftharpoons C - N - K$$

Although both PyPH-HATN CMP-0.75 and PyPH-HATN CMP-1.5 are based on the same redox-active units, the differences in their CV curves could be attributed to variations in polymer network structure and porosity arising from the different monomer ratios. The PyPH-HATN CMP-1.5 sample possesses a more extended network, potentially altering ion accessibility and the electronic conductivity, leading to shifts in peak position, intensity, and shape. These structural differences are supported by our BET surface area and pore size distribution data

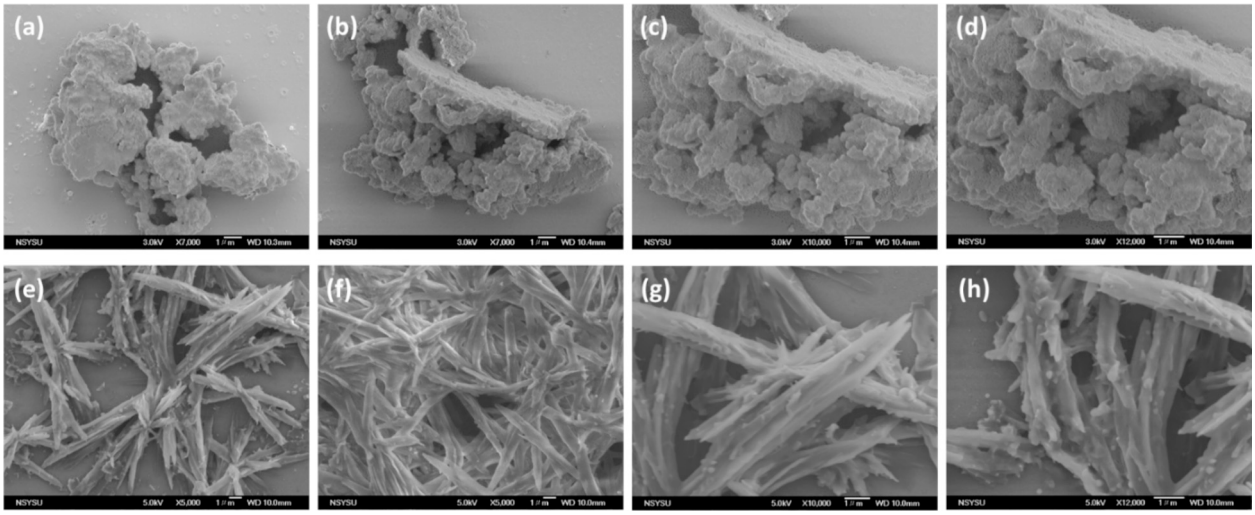

Fig. 3. (a-h) SEM images recorded for the (a-d) PyPH-HATN CMP-0.75 and (e-h) PyPH-HATN CMP-1.5 [Scale bar in all SEM images is 1 μm].

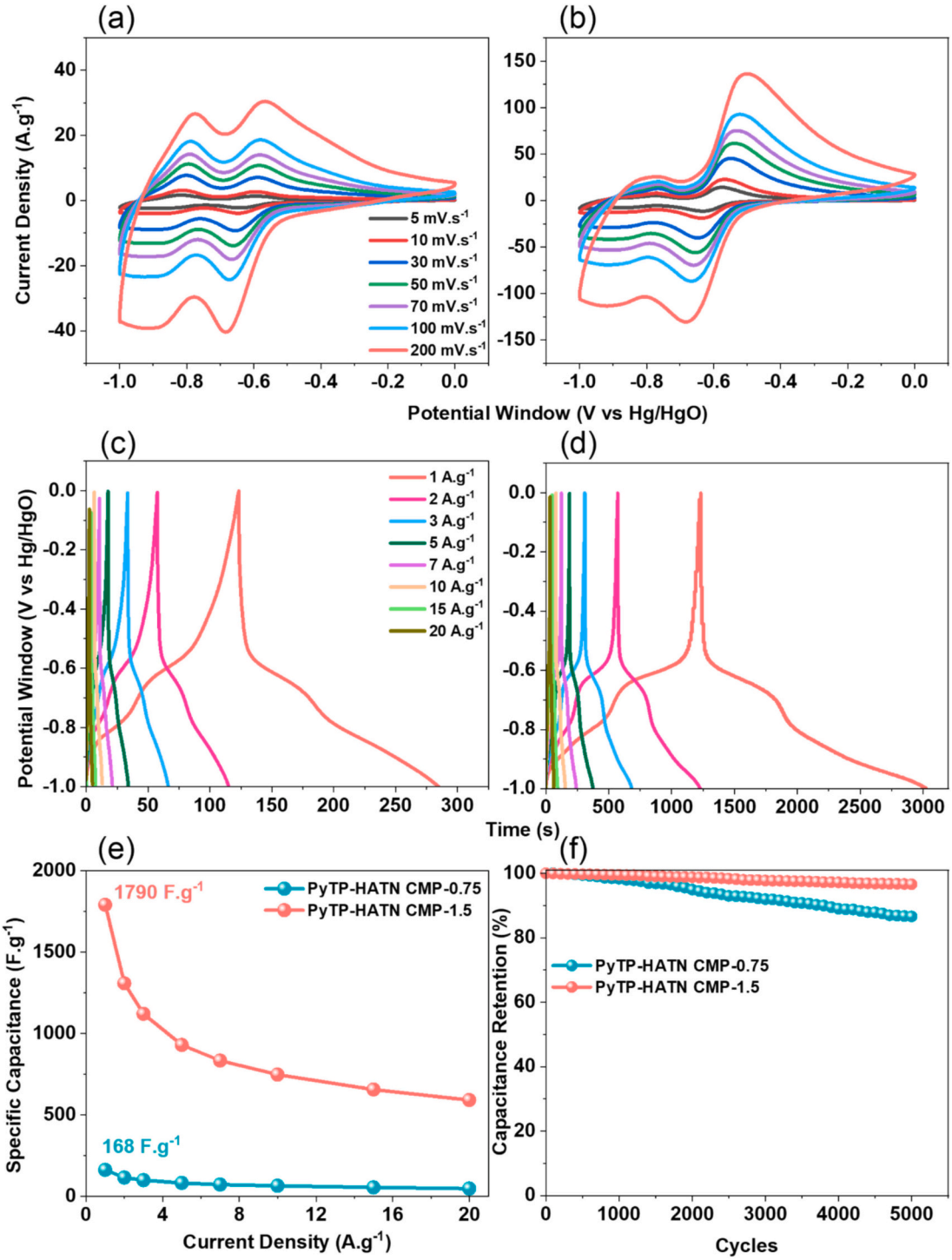

Fig. 4. (a, b) CV profiles, (c, d) GCD profiles, (e) specific capacitance, and (f) capacitance stability of (a, c, e, and f) PyPH-HATN CMP-0.75 and (b, d, e, and f) PyPH-HATN CMP-1.5.

[Fig. 2](f) and Fig. S7], which shows that PyPH-HATN CMP-1.5 is characteristic of *meso* and microporous structures [S_{BET} = 55 $m^2.g^{-1}$], whereas PyPH-HATN CMP-0.75 is indicative of weakly porous material [S_{BET} = 15 $m^2.g^{-1}$]. As such, while the redox-active sites are chemically identical, their electrochemical accessibility and kinetics can vary significantly depending on the polymer network structure and porosity [66].

Thus, to quantify the charge storage feature of the PyPH-HATN CMP-0.75 and PyPH-HATN CMP-1.5 electrodes, the three-electrode cells were subjected to GCD cycling at several current rates at the same fixed voltage. The GCD plots recorded at 1, 2, 3, 5, 7, 10, 15, and 20 $A.g^{-1}$, are shown in Fig. 4(c) and (d). The obtained GCD graphs were very symmetric at all current densities, indicating the strong reversibility of the generated CMP electrodes for charge storage and release. Excellent charge storage capability and robust electrochemical stability are indicated by the almost triangular GCD curves of both electrode materials, which have either constant plateau areas or a slight curvature. The plateau areas imply the persistence of a Faradaic nature, while triangle curves support the presence of EDLC behavior. High coulombic efficiency is also demonstrated by the appearance of extremely symmetric

GCD graphs. Both pseudo-capacity and EDLC characteristics were demonstrated by the triangular, slight bend in the shape of these GCD curves. The specific capacitance of the electrodes was estimated at each current density from the GCD profiles [67]. Therefore, Fig. 4(e) presents the equation that correlates current density with the measured specific capacitance (Csp) for PyPH-HATN CMP-0.75 and PyPH-HATN CMP-1.5 electrodes. Additionally, due to ions present in electrolytes having sufficient time to access the active site of the electroactive CMPs, a rise in capacitance is seen at lower scan rates.

Contrarily, descending scan rates result in a faster electrolyte delivery to the electroactive materials, which reduces capacitance and is seen in the GCD plots. The PyPH-HATN CMP-0.75 and PyPH-HATN CMP-1.5 electrodes exhibited a specific capacitance of 162 and 1790 $F.g^{-1}$ at 1 $A.g^{-1}$. Pseudocapacitive behavior arises due to Faradaic interactions taking place between electrolytes and heteroatoms present on microporous carbon surfaces. The GCD analysis revealed that the PyPH-HATN CMP-1.5 electrode discharge curves showed a longer period of discharge than the PyPH-HATN CMP-0.75 electrode. Interestingly, Csp values 82 $F.g^{-1}$ for PyPH-HATN CMP-0.75 and 930 $F.g^{-1}$ for PyPH-HATN CMP-1.5 were displayed by the electrodes also at 5 $A.g^{-1}$. Thus, suggesting that the active material was fully utilized for charge storage. Notably, PyPH-HATN CMP-1.5 exhibits a higher content of redox-active HATN units, which introduces an increased density of electron-deficient nitrogen sites capable of undergoing reversible faradaic reactions. This structural feature, combined with the rod-like morphology of PyPH-HATN CMP-1.5, significantly facilitates electrolyte ion transport and enhances the accessibility of redox-active sites, thereby markedly improving electrochemical performance. Furthermore, the elevated concentration of nitrogen heteroatoms and HATN moieties contributes to superior specific capacitance, primarily through enhanced electrode–electrolyte interface wettability and the proliferation of electrochemically active sites. Notably, the specific capacitance of PyPH-HATN CMP-0.75 and PyPH-HATN CMP-1.5 electrodes steadily decreased with ascending current density, as electrolyte ions cannot fully migrate through the porous CMPs at higher current densities as for charge storage, only the external active surface is utilized. The cyclic stabilities of PyPH-HATN CMP-0.75 and PyPH-HATN CMP-1.5 electrodes were assessed over 5000 cycles at 20 $A.g^{-1}$. As illustrated in Fig. 4 (f), both PyPH-HATN CMP-0.75 and PyPH-HATN CMP-1.5 electrode materials demonstrated outstanding stability of 87 % and 97 % to their

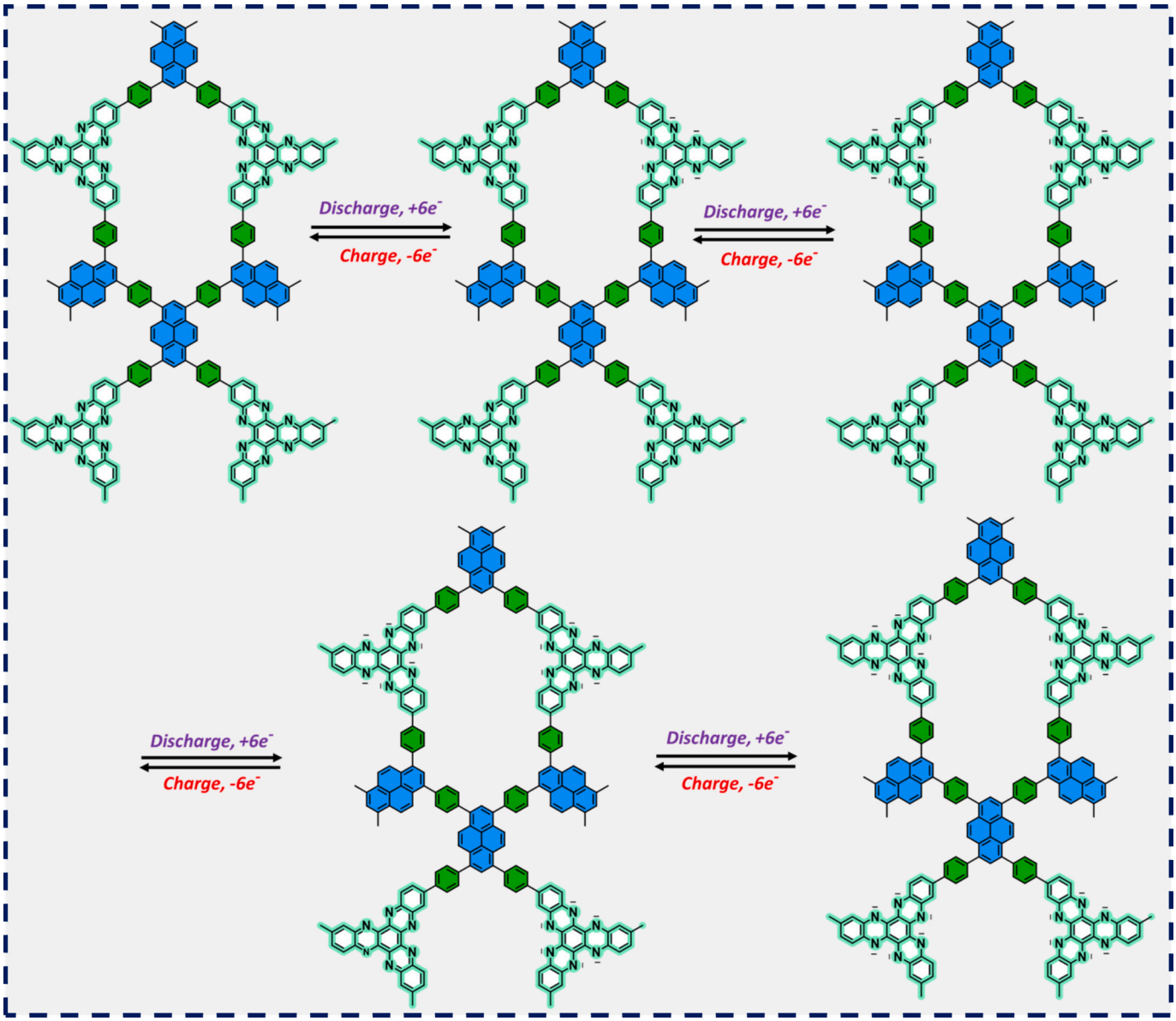

Fig. 5. The possible mechanism of the PyPH-HATN CMP material during the discharge-charge process.

original capacitance, respectively. The proposed mechanism of the PyPH-HATN CMP electrode material during the discharge-charge process is illustrated in Fig. 5. This mechanism suggests that each HATN unit serves as an active redox center capable of accepting up to six electrons in the charging process. During charging, the conjugated structure of the HATN unit facilitates electron transfer, enabling efficient charge storage. The reduction of the HATN core likely occurs in a stepwise manner, with sequential electron uptake leading to the stabilization of intermediate species.

Conversely, in the discharging process, the stored electrons are released, restoring the original oxidation state of the HATN units. This reversible redox activity contributes to the overall electrochemical performance of the PyPH-HATN CMP material, making it a promising candidate for SC applications. A comparison of Csp values of the PyPH-HATN CMP-0.75 and PyPH-HATN CMP-1.5 based organic electrode materials at their respective current densities and the present work are shown in Table S1. Undoubtedly, the reported specific capacitance of PyPH-HATN CMP-1.5 electrode is comparable with the previous literature due to its moderate surface area, porosity, and greater number of N heteroatoms in the HATN units leading to exceptional performance.

Electrochemical impedance spectroscopy (EIS) was used to probe the electrochemical features of PyPH-HATN CMP-0.75 and PyPH-HATN CMP-1.5 electrodes, as illustrated in Fig. 6(a) and (b). EIS is useful for studying the ion and electron motions on the three-electrode setup before and after conducting cycle life tests (5000 cycles), as well as for analysing its impedance behavior across different frequencies and additional electrochemical characteristics like resistance and capacitance [68]. Following fitting the EIS curves, the initial resistances of the PyPH-HATN CMP-0.75 and PyPH-HATN CMP-1.5 electrodes were determined to be 27.47 Ω and 12.57 Ω, respectively. The PyPH-HATN CMP-1.5 electrode showed its benefits as an efficient electrode material by having the least amount of resistance. As seen by the frequency-dependent magnitude Bode curve in Fig. 6(c), PyPH-HATN CMP-0.75 and PyPH-HATN CMP-1.5 exhibit remarkable capacitive properties in energy applications. Fig. 6(d) displays frequency-dependent phase-angle Bode profiles for PyPH-HATN CMP-0.75 and PyPH-HATN CMP-1.5 electrodes, illustrating the knee frequencies that gauge the porous material's performance. The knee frequency emerges when the phase angle reaches 45°, indicating a balance between capacitive and resistive responses. PyPH-HATN CMP-0.75 and PyPH-HATN CMP-1.5 were found to have knee frequencies of 6.64 Hz and 2.10 Hz, respectively. In conclusion, the EIS data showed that both electrodes, particularly PyPH-HATN CMP-1.5 with its low series resistance, possess the ability to be exploited as efficient SC electrode materials.

3.3. *Capacitive and diffusive charge storage in PyPH-HATN CMP-0.75 and PyPH-HATN CMP-1.5 electrodes*

A thorough CV analysis was conducted on a three-electrode setup at different low scan rates to deconvolute the capacitive and diffusive modes of charge storage in the PyPH-HATN CMP-0.75 and PyPH-HATN CMP-1.5, as illustrated in Fig. S10(a) and Fig. 7(a). For both PyPH-HATN CMP-0.75 and PyPH-HATN CMP-1.5, the CV profiles show distinct redox peaks clearly at all low scan rates. Fig. S10(b) and Fig. 7(b) show the Randles-Sevcik plots, which were generated to investigate the impact of scan rate on the corresponding peak currents derived from the CV. The

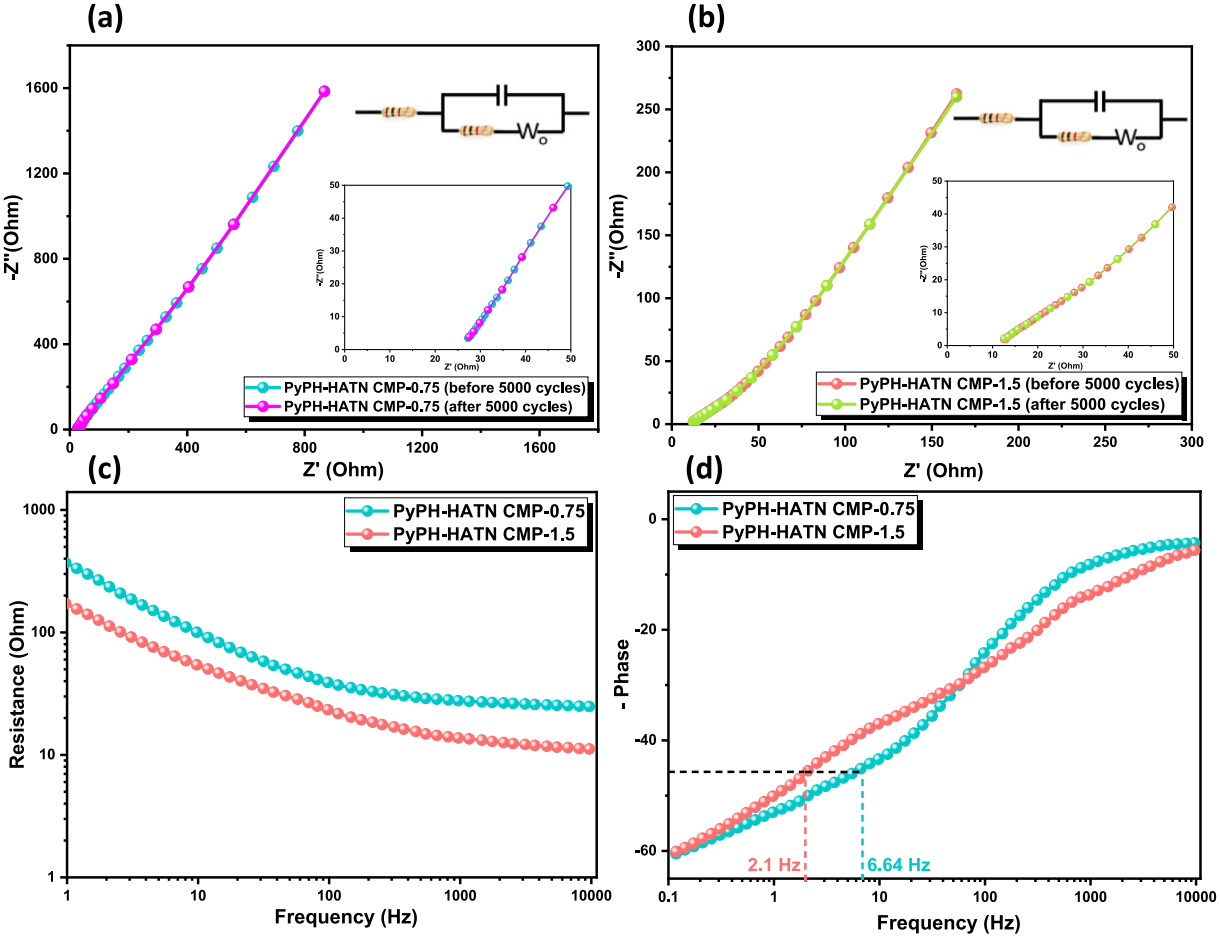

Fig. 6. (a, b) EIS profiles of (a) PyPH-HATN CMP-0.75 and (b) PyPH-HATN CMP-1.5. Insets: Localized enlargement of the Nyquist plots and Equivalent circuit used for fitting, (c) Frequency-dependent magnitude Bode and (d) Frequency-dependent phase-angle Bode graphs for PyPH-HATN CMP-0.75 and PyPH-HATN CMP-1.5.

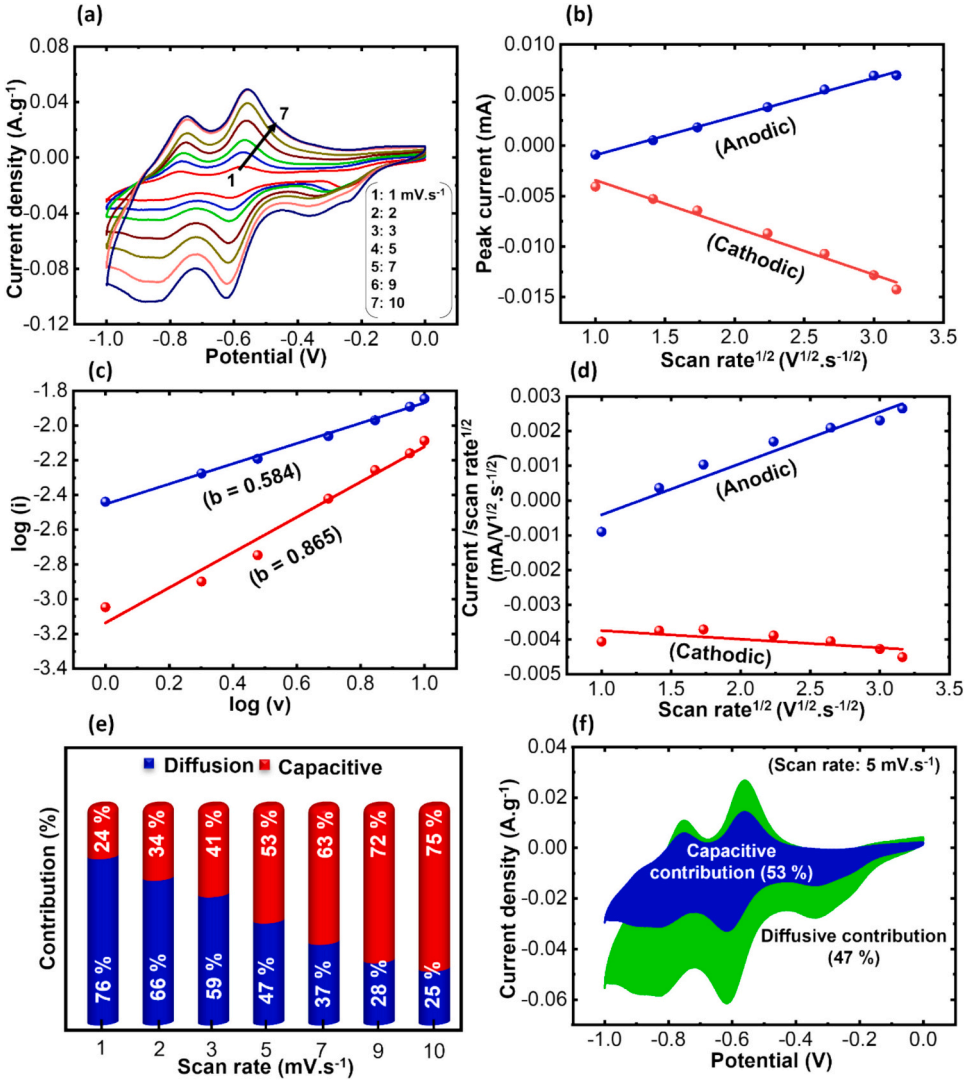

Fig. 7. (a) CV profiles of PyPH-HATN CMP-1.5 for SCs, (b) Randles plot, (c) Power law plot, and (d) Dunn's plot of the PyPH-HATN CMP-1.5. (e) The proportion of capacitive behavior in PyPH-HATN CMP-1.5 under varying scan rates. (f) Contribution from capacitance in the PyPH-HATN CMP-1.5 at 5 $mV.s^{-1}$.

peak current increases linearly with an increase in scan rate, indicating the occurrence of reversible ion diffusion in the PyPH-HATN CMP-0.75 and PyPH-HATN CMP-1.5 electrodes. The capacitive and diffusive charge storage can be distinguished quantitatively using the Power law, as shown below [69]:

$$i = av^b$$

$$\log(i) = \log a + b\log(v)$$

where a and b are constants and i and υ represent the peak current (in A) and scan rate (in $mV.s^{-1}$). The slope of the log(i) vs log(v) linear plot can be used to get the constant b, and the intercept can be used to determine the constant a. If b = 0.5, the electrode is diffusive; if b = 1.0, it is said to be capacitive [70]. The calculated slope values for the anodic and cathodic peaks in the Power-law linear plot are 0.584 and 0.865 for PyPH-HATN CMP-0.75 electrode and 0.590 and 0.981 for PyPH-HATN CMP-1.5 electrode as depicted in Fig. S10(c) and Fig. 7(c), respectively, indicating that the charge storage in PyPH-HATN CMP-0.75 and PyPH-HATN CMP-1.5 electrodes is a combination of capacitive and diffusion mode charge storage, with the diffusive mode predominating. Additionally, the percentage contributions of the diffusive capacitances and the double layer were measured using Dunn's approach. It states that both capacitive and diffusive contributions make up the total current, i, in the CV profile at any potential, as shown below [71]:

$$i(v) = i_{cap} + i_{diff}$$

$$i(v) = k_1 v + k_2 v^{1/2} \text{ or } \frac{i(v)}{v^{1/2}} = k_1 v^{\frac{1}{2}} + k_2$$

where k_1 and k_2 are constants, i(v) represents the total current, i_{cap} represents the capacitive current contribution attained because of double-layer (DL) storage, and i_{diff} represents the diffusive current contribution as a result of the Faradaic reactions. For the anodic and cathodic response, Fig. S10(d) and Fig. 7(d) show Dunn's plot, which is a linear plot of ($i/v^{1/2}$) vs ($v^{1/2}$). The corresponding capacitive and diffusive current contributions were assessed at different scan rates based on the slope values. Fig. S10(e) and Fig. 7(e) present a bar diagram that illustrates the contributions. The diffusion was as high as 76 % for the PyPH-HATN CMP-0.75 electrode and 75 % for the PyPH-HATN CMP-1.5 electrode at 1 $mV.s^{-1}$, validating the diffusive method of charge storage. Significant capacitive contributions could reach up to 63 % for the PyPH-HATN CMP-0.75 electrode and 66 % for the PyPH-HATN CMP-1.5 electrode, whereas the diffusive contribution decreased to 37 % for the PyPH-HATN CMP-0.75 electrode and 34 % for the PyPH-HATN CMP-1.5 electrode at 7 $mV.s^{-1}$. The CV profile for PyPH-HATN CMP-0.75 and PyPH-HATN CMP-1.5 electrodes,

respectively, was obtained at 5 mV.s^{-1}, shows contributions of the diffusive (47.44 %) and capacitive (53.56 %) types in Fig. S10(f) and Fig. 7(f). At low frequencies, ion transport through the electrode active materials is evident. The following equation was used to get the diffusion coefficient of the ions from the low-frequency region of the EIS spectra [66]:

$$D = \frac{R^2T^2}{2A^2n^4F^4C2\sigma^2}$$

where A stands for the electrode area, n for the number of electrons, F for the Faraday constant, C for the initial concentration, R for the gas constant, T for the absolute temperature, and σ for the Warburg factor. The following equation, in which ω stands for the angular frequency in the low-frequency area, is associated with the Warburg factor [72]:

$$Z' \propto \sigma\omega^{-1/2}$$

The slope of this linear equation of Z′ and $\omega^{-1/2}$ corresponds to the Warburg factor (σ), which is connected to the ion diffusion in the electrode material. The computed σ for the PyPH-HATN CMP-0.75 and PyPH-HATN CMP-1.5 electrodes is 744.67 and 237.35, respectively, as illustrated in Figs. S11(a) and S11(b). As a result, the diffusion coefficient ($D_{\overline{OH}}$) values for the ions in PyPH-HATN CMP-0.75 and PyPH-

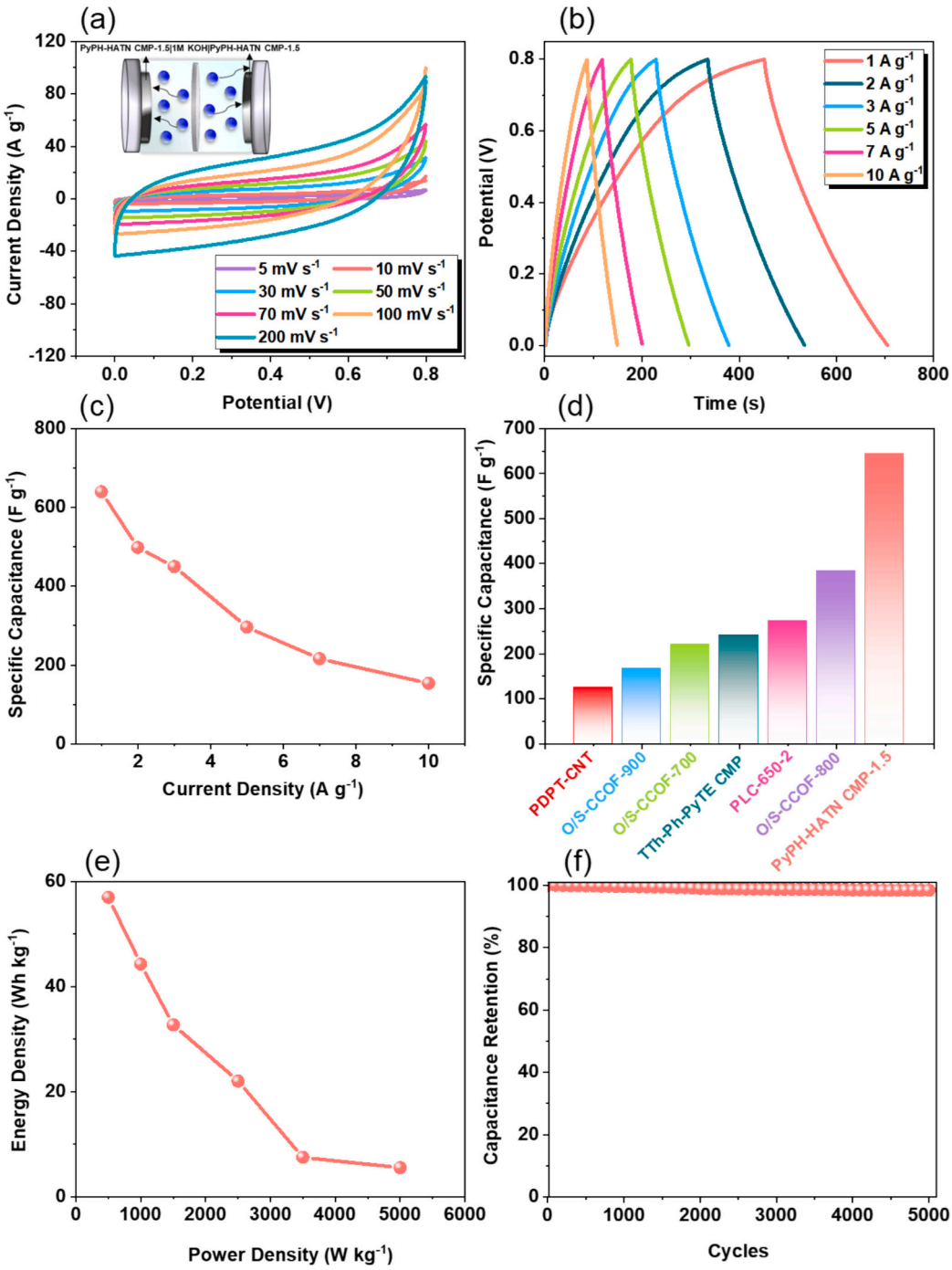

Fig. 8. (a) CV, Inset: Schematic of coin cell SC using symmetric PyPH-HATN CMP-1.5 electrodes (b) GCD, and (c) specific capacitance profiles of PyPH-HATN CMP-1.5, (d) comparison of SCs performance of PyPH-HATN CMP-1.5 compared with other reported materials, (e) Ragone plot and (f) capacitance stability plots of PyPH-HATN CMP-1.5.

HATN CMP-1.5 electrodes are 1.29×10^{-11} and 1.27×10^{-10} $cm^2.s^{-1}$, respectively. The higher diffusion coefficient of PyPH-HATN CMP-1.5 can be attributed to factors like enhanced ion transport pathways due to the rod-like morphology of the PyPH-HATN CMP-1.5 as compared to PyPH-HATN CMP-0.75, which facilitates faster electrolyte ion diffusion, improving ionic mobility within the electrode material. The increased HATN content in PyPH-HATN CMP-1.5 introduces more electrochemically active nitrogen sites, enhancing ion-electron interactions. This led to improved charge accommodation and faster redox kinetics, contributing to a slightly higher diffusion coefficient. Further, for practical applicability, two-electrode symmetric SC in the form of CR-2032 were fabricated employing the PyPH-HATN CMP-1.5 electrode material over a potential range of 0–0.8 V, as displayed in Fig. 8(a). It is seen that all the CV curves show a nearly rectangular form accompanied with humps representing typical double layer (DL) and pseudocapacitive characteristics. As the scan rate increases, the current response in the CV profiles rises as well, suggesting that the PyPH-HATN CMP-1.5 electrode has good rate capability and electrode stability, two qualities that are favorable for SCs applications. GCD profiles at a range of current densities from 1 to 10 $A.g^{-1}$ within the fixed potential window as shown in Fig. 8(b) were used to calculate the Csp of the PyPH-HATN CMP-1.5 electrode. The nearly triangular curves show the effects of both electric DL capacitance and pseudo-capacitance, due to the presence of heteroatoms in the PyPH-HATN CMP-1.5 electrode, causing an asymmetric curve. Based on the GCD curves, the C_{sp} of the PyPH-HATN CMP-1.5 electrode was 640 $F.g^{-1}$, respectively, at a 1 $A.g^{-1}$ as seen in Fig. 8(c). Remarkably, Fig. 8(d) highlights that the symmetric PyPH-HATN CMP-1.5-coin cell achieved the highest C_{sp}, outperforming previously reported electrodes such as PDPT-CNT [73], O/S-CCOF-900 [74], O/S-CCOF-700 [74], TTh-Ph-PyTE CMP [23], PLC-650-2 [75], and O/S-CCOF-800 [74]. Additionally, the energy density of PyPH-HATN CMP-1.5 (57.4 $Wh.kg^{-1}$) [Fig. 8(e)]. Furthermore, we evaluated the cycling stability at 10 $A.g^{-1}$ for 5000 cycles for PyPH-HATN CMP-1.5 [Fig. 8(f)], the PyPH-HATN CMP-1.5 electrode (98.57 %) had a greater capacity retention rate.

Thus, the PyPH-HATN CMP-1.5 electrode offered higher specific capacitance and better overall performance. Impedance analysis was performed on the coin cells to investigate the ion/electron transit. In Fig. S12(a), the resulting Nyquist plots (raw and fitted) are displayed for the PyPH-HATN CMP-1.5 with the equivalent circuit (inset) used to fit the curves. The Nyquist plots have a 45° angled spike to the *x*-axis in the low-frequency zone, suggesting a capacitive nature for charge storage, and a semicircle in the high-frequency region, suggesting the electrode/electrolyte resistance. The solution resistances of the PyPH-HATN CMP-1.5 were 5.44 Ω, whereas its corresponding charge-transfer resistances was 10.37 Ω, respectively. Fig. S12(b) illustrates the magnitude Bode plots as a function of frequency, exhibiting insignificant resistance at higher frequencies and inclined lines with a negative gradient in the low-frequency region. For a phase angle of 45°, the knee frequencies for PyPH-HATN CMP-1.5 were determined to be 18.04 Hz, respectively, based on the frequency-dependent phase angle graphs shown in Fig. S12 (c). Thus, the lower solution and charge-transfer resistance of PyPH-HATN CMP-1.5 offered higher specific capacitance and better overall performance. Ex-situ FTIR analyses were performed on symmetric PyPH-HATN CMP-0.75 and PyPH-HATN CMP-1.5 coin cells after 5000 charge–discharge cycles (Fig. S13). The spectra revealed minimal changes compared to the initial state, indicating that both the structural and chemical frameworks of the PyPH-HATN CMP-0.75 and PyPH-HATN CMP-1.5 electrodes remained largely unaltered throughout prolonged electrochemical cycling. These results affirm the excellent chemical stability and robustness of the CMP materials under repeated redox conditions. To evaluate the structural integrity and elucidate the reaction mechanism of the PyPH-HATN CMP-based electrodes, CR2032-type coin cells incorporating PyPH-HATN CMP-0.75 and PyPH-HATN CMP-1.5 were disassembled after 5000 charge–discharge cycles. SEM analysis of the cycled electrodes [Fig. S14] revealed notable differences in morphological evolution. The PyPH-HATN CMP-1.5 electrode, which initially exhibited a rod-like morphology, transformed into thermodynamically favorable spherical aggregates. This restructuring is attributed to repeated and reversible redox processes, as schematically illustrated in Fig. 5. In contrast, the PyPH-HATN CMP-0.75 electrode retained a morphology closely resembling its pristine state, with no significant structural degradation. The preserved appearance suggests enhanced molecular mobility under electrochemical cycling conditions, which may facilitate reorganization and densification, ultimately yielding a more porous structure. The excellent long-term cycling stability observed for both electrodes is primarily ascribed to the intrinsic robustness of the CMP frameworks. Their highly porous and π-conjugated architectures afford substantial free volume, enabling efficient ion diffusion and electron transport throughout extended cycling. Notably, although PyPH-HATN CMP-1.5 experienced morphological evolution from rods to agglomerated spheres, the continuity of the electroactive polymer network remained intact. This structural preservation underpins the sustained electrochemical performance and high capacitance retention observed over prolonged operation. Density functional theory (DFT) calculations were conducted for both building blocks [Py and HATN] as well as the PyPH-HATN CMP to elucidate their geometric structures and electronic properties. The highest occupied molecular orbital (HOMO) and lowest unoccupied molecular orbital (LUMO), along with their corresponding energy levels, were computed using the B3LYP-D3(BJ)/6-31G(d) method. The optimized geometry of Py and HATN shows that both molecules are perfectly planar. The Py and HATN moieties in the PyPH-HATN CMP have torsional angles of 54.0 and 35.4 to the benzene ring. Fig. S15 presents the HOMO-LUMO isosurface maps of Py, HATN, and PyPH-HATN CMP. Both building units [Py, HATN] are completely conjugated, with both HOMO and LUMO spread over the entire conjugated system. The HOMO-LUMO energy gap is 3.857 eV for Py and 3.77 eV for HATN. The HOMO is the part that donates electrons because it has the electrons with the highest energy. LUMO, on the other hand, is the electron-accepting region. In Fig. S15, the HOMO of Py has higher energy than HATN. Moreover, the LUMO of HATN has lower energy than Py. These results show that Py is a better electron donor and HATN is a better acceptor. In the PyPH-HATN CMP, HOMO and LUMO are located in two different regions. The HOMO is located on the Py moiety, with no contribution from the HATN system. The LUMO, on the other hand, consists entirely of the HATN. This is reflected in the energies of the HOMO and LUMO of the polymer. The PyPH-HATN CMP has a HOMO energy of −5.29 eV, only 0.04 eV higher than the Py ring. The PyPH-HATN CMP has the same energy for LUMO as HATN, −2.63 eV. This led to the reduction of the HOMO-LUMO gap of the PyPH-HATN CMP to 2.66 eV. The small gap of the PyPH-HATN CMP indicates that it is more reactive than both building units. This distribution of the HOMO and LUMO, on two different parts of the PyPH-HATN CMP, shows that excitation will be followed by electronic charge transfer from Py to the HATN moiety. Moreover, the small energy gap between the two orbitals facilitates the charge transfer and leads to improving the SCs application for PyPh-HATN CMP [76]. The electronic charge will be delocalized over the molecule forming a molecular conductor. Fig. S16 shows the molecular electrostatic potential (MESP) analysis of the building units and the PyPH-HATN CMP. This plot gives a numerical expression of the electrophilic and nucleophilic sites and thus shows the most reactive sites, within a molecule. The red color shows the areas with the highest electron density; low electron densities are depicted by a blue color. In Py, high electron densities (areas with dense red color) are around the π-electrons of the rings. These are the areas with the highest negative potential. The terminal hydrogens of the aromatic rings have the highest positive potential. For HATN, the highest negative ESP is −49 kcal/mol and is produced by the lone pairs of nitrogen atoms.

4. Conclusions

In this study, we successfully developed unique PyPH-HATN CMP-

1.5, via Suzuki coupling, deliberately incorporating redox-active HATN moieties to enhance their functionality as organic electrode materials with high efficiency for next-generation supercapacitors. Morphological analysis unveiled that PyPH-HATN CMP-1.5 featured a well-defined rod-like framework, intricately engineered with a highly interconnected network of pores. Electrochemical assessments demonstrated that the PyPH-HATN CMP-1.5 electrode exhibited an exceptionally high Csp of 1790 $F.g^{-1}$ at 1 $A.g^{-1}$, attributed to its well-engineered porosity, heteroatom-rich composition, and optimized structural attributes. Notably, even at an elevated 20 $A.g^{-1}$, the PyPH-HATN CMP-1.5 electrode retained a commendable Csp of 640 $F.g^{-1}$. Furthermore, the PyPH-HATN CMP-1.5 electrode demonstrated outstanding long-term electrochemical stability, maintaining 97 % of its initial capacitance after 5000 charge-discharge cycles. Beyond its superior electrochemical performance, PyPH-HATN CMP-1.5 electrode exhibited a pronounced diffusive charge storage mechanism, with up to 75 % diffusion-controlled contribution at 1 $mV.s^{-1}$ and a diffusion coefficient of 1.27×10^{-10} $cm^2.s^{-1}$. These findings underscore the immense potential of PyPH-HATN CMP-1.5 as promising candidates for next-generation SCs applications, because of the facile synthetic approach, rich HATN units, and tunable morphology.

CRediT authorship contribution statement

Mohamed Gamal Mohamed: Writing – review & editing, Writing – original draft, Supervision, Methodology, Investigation, Formal analysis, Data curation, Conceptualization. **Bhargabi Halder:** Writing – original draft, Investigation, Data curation. **Poonam Nagendra Singh:** Formal analysis, Data curation. **Ahmed A.K. Mohammed:** Formal analysis. **Perumal Elumalai:** Supervision, Project administration. **Shiao-Wei Kuo:** Supervision, Resources, Funding acquisition.

Declaration of competing interest

The authors declare that they have no known competing financial interests or personal relationships that could have appeared to influence the work reported in this paper.

Acknowledgments

This study was supported financially by the National Science and Technology Council, Taiwan, under contracts NSTC 113-2223-E-110-001- and 113-2221-E-110-012-MY3. The authors thank the Science and Engineering Research Board (SERB), Government of India, under the research grant (CRG/2021/005678) and Central Power Research Institute, Bangalore (CPRI) under the research grant (CPRI/R&D/TC/GDEC/2023). The authors thank the staff at National Sun Yat-sen University for their assistance with the TEM (ID: EM022600) experiments.

Appendix A. Supplementary data

Supplementary data to this article can be found online at https://doi.org/10.1016/j.cej.2025.165892.

Data availability

Data will be made available on request.

References

[1] S.K. Fayegh, M.A. Rosen, A review of energy storage types, applications and recent developments, J Energy Storage 27 (2020) 101047, https://doi.org/10.1016/j.est.2019.101047.
[2] Y. Chen, Z. Song, Y. Lv, L. Gan, M. Liu, NH_4^+-modulated cathodic interfacial spatial charge redistribution for high-performance dual-ion capacitors, Nano-Micro Lett. 17 (2025) 117, https://doi.org/10.1007/s40820-025-01660-0.
[3] S.Y. Chang, A.M. Elewa, M.G. Mohamed, I.M.A. Mekhemer, M.M. Samy, K. Zhang, H.H. Chou, S.W. Kuo, Rational design and synthesis of bifunctional dibenzo [g,p] chrysene-based conjugated microporous polymers for energy storage and visible light-driven photocatalytic hydrogen evolution, Mater. Today Chem. 33 (2023) 101680, https://doi.org/10.1016/j.mtchem.2023.101680.
[4] A.O. Mousa, C.H. Chuang, S.W. Kuo, M.G. Mohamed, Strategic design and synthesis of ferrocene linked porous organic frameworks toward tunable CO_2 capture and energy storage, Int. J. Mol. Sci. 24 (2023) 12371, https://doi.org/10.3390/ijms241512371.
[5] X. Yang, C. Hu, Y. Chen, Z. Song, L. Miao, Y. Lv, H. Duan, M. Liu, L. Gan, Tailoring ion-accessible pores of robust nitrogen heteroatomic carbon nanoparticles for high-capacity and long-life Zn-ion storage, J Energy Storage 104 (2024) 114509, https://doi.org/10.1016/j.est.2024.114509.
[6] B. Halder, M.G. Mohamed, S.W. Kuo, P. Elumalai, Review on composite polymer electrolyte using PVDF-HFP for solid-state lithium-ion battery, Mater. Today Chem. 36 (2024) 101926, https://doi.org/10.1016/j.mtchem.2024.101926.
[7] A.G. Olabi, Q. Abbas, A. Al Makky, M.A. Abdelkareem, Supercapacitors as next generation energy storage devices: properties and applications, Energy 248 (2022) 123617, https://doi.org/10.1016/j.energy.2022.123617.
[8] P.A. Østergaard, N. Duic, Y. Noorollahi, H. Mikulcic, S. Kalogirou, Sustainable development using renewable energy technology, Renew. Energy 146 (2020) 2430–2437, https://doi.org/10.1016/j.renene.2019.08.094.
[9] X. Zheng, Z. Song, D. Zhang, W. Du, L. Miao, Y. Lv, L. Xie, L. Gan, M. Liu, Rational design of a dual-gradient zincophilic–conductive interphase for dendrite-free zinc batteries, J Mater Chem A 12 (2024) 15352–15360, https://doi.org/10.1039/D4TA02639J.
[10] A. Basit, M.G. Mohamed, S.U. Sharma, S.W. Kuo, Thianthrene- and thianthrene tetraoxide-functionalized conjugated microporous polymers for efficient energy storage, ACS Appl. Polym. Mater. 6 (2024) 12247–12260, https://doi.org/10.1021/acsapm.4c02368.
[11] P. Simon, Y. Gogotsi, B. Dunn, Where do batteries end and supercapacitors begin? Science 343 (2014) 6176, https://doi.org/10.1126/science.1249625.
[12] J.C. Gutiérrez, A. Celzard, V. Fierro, Energy storage in supercapacitors: focus on tannin-derived carbon electrodes, Front. Mater. 7 (2020) 217, https://doi.org/10.3389/fmats.2020.00217.
[13] A. Basit, M.G. Mohamed, M. Ejaz, B.X. Su, H. Manzoor, S.W. Kuo, Boosting supercapacitor energy storage using microporous carbon derived from an octavinylsilsesquioxane and fluorenone-linked porous hybrid polymer, ACS Appl Energy Mater 7 (2024) 7505–7516, https://doi.org/10.1021/acsaem.4c01796.
[14] M.M. Samy, M.G. Mohamed, S.U. Sharma, S.V. Chaganti, J.T. Lee, S.W. Kuo, An ultrastable tetrabenzonaphthalene-linked conjugated microporous polymer functioning as a high-performance electrode for supercapacitors, J. Taiwan Inst. Chem. Eng. 158 (2024) 104750, https://doi.org/10.1016/j.jtice.2023.104750.
[15] W. Lyu, W. Zhang, H. Liu, Y. Liu, H. Zuo, C. Yan, C.F.J. Faul, A. Thomas, M. Zhu, Y. Liao, Conjugated microporous polymer network grafted carbon nanotube fibers with tunable redox activity for efficient flexible wearable energy storage, Chem. Mater. 32 (2020) 8276–8285, https://doi.org/10.1021/acs.chemmater.0c02089.
[16] B. Halder, S. Ragul, S. Sandhiya, P. Elumalai, Flexible solid-state aqueous sodium-ion capacitor using mesoporous self-heteroatom-doped carbon electrodes, ACS Appl. Electron. Mater. 5 (2023) 470–483, https://doi.org/10.1021/acsaelm.2c01474.
[17] M.G. Mohamed, S.U. Sharma, P.T. Wang, M. Ibrahim, M.H. Lin, C.L. Liu, M. Ejaz, H.J. Yen, S.W. Kuo, Construction of fully π-conjugated, diyne-linked conjugated microporous polymers based on tetraphenylethene and dibenzo [g, p] chrysene units for energy storage, Polym. Chem. 15 (2024) 2827–2839, https://doi.org/10.1039/D4PY00421C.
[18] M.G. Mohamed, B.X. Su, S.W. Kuo, Robust nitrogen-doped microporous carbon via crown ether-functionalized benzoxazine-linked porous organic polymers for enhanced CO_2 adsorption and supercapacitor applications, ACS Appl. Mater. Interfaces 16 (2024) 40858–40872, https://doi.org/10.1021/acsami.4c05645.
[19] M.G. Mohamed, M. Ibrahim, N.P. Chen, A. Basit, Y.C. Kao, A.O. Mousa, M. M. Samy, S.W. Kuo, Tetrabenzonaphthalene and redox-active anthraquinone-linked conjugated microporous polymers as organic electrodes for enhanced energy storage efficiency, ACS Appl Energy Mater 7 (2024) 5582–5593, https://doi.org/10.1021/acsaem.4c01276.
[20] L. Guan, L. Yu, G.Z. Chen, Capacitive and non-capacitive faradaic charge storage, Electrochim. Acta 206 (2016) 464–478, https://doi.org/10.1016/j.electacta.2016.01.213.
[21] A.O. Mousa, S.U. Sharma, S.V. Chaganti, T.H. Mansoure, P.N. Singh, M. Ejaz, C. H. Chuang, J.T. Lee, S.W. Kuo, M.G. Mohamed, Designing strategically functionalized conjugated microporous polymers with pyrene and perylenetetracarboxylic dianhydride moieties with single-walled carbon nanotubes to enhance supercapacitive energy storage efficiency, J. Power Sources 608 (2024) 234624, https://doi.org/10.1016/j.jpowsour.2024.234624.
[22] D.P. Chatterjee, A.K. Nandi, A review on the recent advances in hybrid supercapacitors, J Mater Chem A 9 (2021) 15880–15918, https://doi.org/10.1039/D1TA02505H.
[23] S.V. Chaganti, S.U. Sharma, M. Ibrahim, A. Basit, P.N. Singh, S.W. Kuo, M. G. Mohamed, Redox-active a pyrene-4,5,9,10-tetraone and thienyltriazine-based conjugated microporous polymers for boosting faradaic supercapacitor energy storage, J. Power Sources 627 (2025) 235848, https://doi.org/10.1016/j.jpowsour.2024.235848.
[24] A. Mauger, C. Julien, A. Paolella, M. Armand, K. Zaghib, Recent progress on organic electrodes materials for rechargeable batteries and supercapacitors, Materials 12 (2019) 1770, https://doi.org/10.3390/ma12111770.

[25] W. Ding, L. Xiao, L. Lv, Y. Wang, Redox-active organic electrode materials for supercapacitors, Batteries Supercaps 6 (2023) e202300278, https://doi.org/10.1002/batt.202300278.
[26] A. Hayat, M. Sohail, A. El Jery, K.M. Al-Zaydi, S. Raza, H. Ali, Y. Al-Hadeethi, T. A. Taha, I.U. Din, M. Ali Khan, M.A. Amin, E. Ghasali, Y. Orooji, Z. Ajmal, M. Z. Ansari, Recent advances in ground-breaking conjugated microporous polymers-based materials, their synthesis, modification and potential applications, Mater. Today 64 (2023) 180–208, https://doi.org/10.1016/j.mattod.2023.02.025.
[27] M.G. Mohamed, M.M. Samy, T.H. Mansoure, S.U. Sharma, M.S. Tsai, J.H. Chen, J. T. Lee, S.W. Kuo, Dispersions of 1,3,4-oxadiazole-linked conjugated microporous polymers with carbon nanotubes as a high-performance electrode for supercapacitors, ACS Appl Energy Mater 5 (2022) 3677–3688, https://doi.org/10.1021/acsaem.2c00100.
[28] F. Vilela, K. Zhang, M. Antonietti, Conjugated porous polymers for energy applications, Energy Environ. Sci. 5 (2012) 7819, https://doi.org/10.1039/c2ee22002d.
[29] A. Basit, Y.C. Kao, Y. El-Ossaily, S.W. Kuo, M.G. Mohamed, Rational engineering and synthesis of pyrene and thiazolo[5,4-d]thiazole-functionalized conjugated microporous polymers for efficient supercapacitor energy storage, J Mater Chem A 12 (2024) 30508–30521, https://doi.org/10.1039/D4TA05908E.
[30] M.G. Mohamed, A.F.M. EL-Mahdy, M.G. Kotp, S.W. Kuo, Advances in porous organic polymers: syntheses, structures, and diverse applications, Mater. Adv. 3 (2022) 707–733, https://doi.org/10.1039/D1MA00771H.
[31] J.S.M. Lee, A.I. Cooper, Advances in conjugated microporous polymers, Chem. Rev. 120 (2020) 2171–2214, https://doi.org/10.1021/acs.chemrev.9b00399.
[32] X. Liu, C.F. Liu, S. Xu, T. Cheng, S. Wang, W.Y. Lai, W. Huang, Porous organic polymers for high-performance supercapacitors, Chem. Soc. Rev. 29 (2022) 3181–3225, https://doi.org/10.1039/d2cs00065b.
[33] K. Amin, N. Ashraf, L. Mao, C.F.J. Faul, Z. Wei, Conjugated microporous polymers for energy storage: recent progress and challenges, Nano Energy 85 (2021) 105958, https://doi.org/10.1016/j.nanoen.2021.105958.
[34] S.U. Sharma, M.H. Elsayed, I.M.A. Mekhemer, T.S. Meng, H.H. Chou, S.W. Kuo, M. G. Mohamed, Rational design of pyrene and thienyltriazine-based conjugated microporous polymers for high-performance energy storage and visible-light photocatalytic hydrogen evolution from water, Giant 17 (2024) 100217, https://doi.org/10.1016/j.giant.2023.100217.
[35] M.G. Mohamed, C.C. Chen, M. Ibrahim, A.O. Mousa, M.H. Elsayed, Y. Ye, S.W. Kuo, Tetraphenylanthraquinone and dihydroxybenzene-tethered conjugated microporous polymer for enhanced CO_2 uptake and supercapacitive energy storage, JACS Au 4 (2024) 3593–3605, https://doi.org/10.1021/jacsau.4c00537.
[36] A.O. Mousa, Z.I. Lin, S.V. Chaganti, C.H. Chuang, C.K. Chen, S.W. Kuo, M. G. Mohamed, Bifunctional imidazolium linked tetraphenylethene based conjugated microporous polymers for dynamic antibacterial properties and supercapacitor electrodes, Polym. Chem. 15 (2024) 397–411, https://doi.org/10.1039/D3PY01303K.
[37] X. Guan, Y. Zhao, H. Pei, M. Zhao, Y. Wang, X. Zhou, M.G. Mohamed, S.W. Kuo, Y. Ye, Metalloporphyrin conjugated porous polymer in-situ grown on a Celgard separator as multifunctional polysulfide barrier and catalyst for high-performance Li-S batteries, Chem. Eng. J. 473 (2023) 144733, https://doi.org/10.1016/j.cej.2023.144733.
[38] B. Zhang, W. Wang, L. Liang, Z. Xu, X. Li, S. Qiao, Prevailing conjugated porous polymers for electrochemical energy storage and conversion: lithium-ion batteries, supercapacitors and water-splitting, Coord. Chem. Rev. 436 (2021) 213782, https://doi.org/10.1016/j.ccr.2021.213782.
[39] M.G. Mohamed, M.H. Elsayed, C.J. Li, A.E. Hassan, I.M.A. Mekhemer, A.F. Musa, M.K. Hussien, L.C. Chen, K.H. Chen, H.H. Chou, S.W. Kuo, Reticular design and alkyne bridge engineering in donor–π–acceptor type conjugated microporous polymers for boosting photocatalytic hydrogen evolution, J Mater Chem A 12 (2024) 7693–7710, https://doi.org/10.1039/D3TA07309B.
[40] M.G. Mohamed, H.Y. Hu, S. Santhoshkumar, M. Madhu, T.H. Mansoure, C. W. Hsiao, Y. Ye, C.W. Huang, W.L. Tseng, S.W. Kuo, Design and synthesis of bifunctional conjugated microporous polymers containing tetraphenylethene and bisulfone units for energy storage and fluorescent sensing of p-nitrophenol, Colloids Surf. A Physicochem. Eng. Asp. 680 (2024) 132675, https://doi.org/10.1016/j.colsurfa.2023.132675.
[41] M.G. Mohamed, S.U. Sharma, C.H. Yang, M.M. Samy, A.A.K. Mohammed, S. V. Chaganti, J.T. Lee, S.W. Kuo, Anthraquinone-enriched conjugated microporous polymers as organic cathode materials for high-performance lithium-ion batteries, ACS Appl Energy Mater 4 (2021) 14628–14639, https://doi.org/10.1021/acsaem.1c03270.
[42] Y. Xu, S. Jin, H. Xu, A. Nagai, D. Jiang, Conjugated microporous polymers: design, synthesis and application, Chem. Soc. Rev. 42 (2013) 8012, https://doi.org/10.1039/c3cs60160a.
[43] M. Ejaz, M.G. Mohamed, W.C. Huang, S.W. Kuo, Pyrene-based covalent organic polymers with nano carbonaceous composites for efficient supercapacitive energy storage, J Mater Chem A 11 (2023) 22868–22883, https://doi.org/10.1039/D3TA02741D.
[44] M.G. Mohamed, S.V. Chaganti, S.U. Sharma, M.M. Samy, M. Ejaz, J.T. Lee, K. Zhang, S.W. Kuo, Constructing conjugated microporous polymers containing the pyrene-4,5,9,10-tetraone unit for energy storage, ACS Appl Energy Mater 5 (2022) 10130–10140, https://doi.org/10.1021/acsaem.2c01842.
[45] M.M. Samy, M.G. Mohamed, S.W. Kuo, Pyrene-functionalized tetraphenylethylene polybenzoxazine for dispersing single-walled carbon nanotubes and energy storage, Compos. Sci. Technol. 199 (2020) 108360, https://doi.org/10.1016/j.compscitech.2020.108360.
[46] A.O. Mousa, M.G. Mohamed, Z.I. Lin, C.H. Chuang, C.K. Chen, S.W. Kuo, Construction of cationic conjugated microporous polymers containing pyrene units through post-cationic modification for enhanced antibacterial performance, J. Taiwan Inst. Chem. Eng. 157 (2024) 105448, https://doi.org/10.1016/j.jtice.2024.105448.
[47] A.O. Mousa, M.G. Mohamed, C.H. Chuang, S.W. Kuo, Carbonized aminal-linked porous organic polymers containing pyrene and triazine units for gas uptake and energy storage, Polymers 15 (2023) 1891, https://doi.org/10.3390/polym15081891.
[48] M.G. Mohamed, T.H. Mansoure, M.M. Samy, Y. Takashi, A.A.K. Mohammed, T. Ahamad, S.M. Alshehri, J. Kim, B.M. Matsagar, K.C.W. Wu, S.W. Kuo, Ultrastable conjugated microporous polymers containing benzobisthiadiazole and pyrene building blocks for energy storage applications, Molecules 27 (2022) 2025, https://doi.org/10.3390/molecules27062025.
[49] Y. Zhao, F. Xie, C. Zhang, R. Kong, S. Feng, J.X. Jiang, Porous carbons derived from pyrene-based conjugated microporous polymer for supercapacitors, Microporous Mesoporous Mater. 240 (2017) 73–79, https://doi.org/10.1016/j.micromeso.2016.10.048.
[50] P.N. Singh, M.G. Mohamed, S.V. Chaganti, S.U. Sharma, M. Ejaz, J.T. Lee, S. W. Kuo, Rational design of ultrastable conjugated microporous polymers based on pyrene and perylene units as high-performance organic electrode materials for supercapacitor applications, ACS Appl Energy Mater 6 (2023) 8277–8287, https://doi.org/10.1021/acsaem.3c01391.
[51] X.Y. Yan, M.D. Lin, S.T. Zheng, T.G. Zhan, X. Zhang, K.D. Zhang, X. Zhao, Recent advances of hexaazatriphenylene (HAT) derivatives: their applications in self-assembly and porous organic materials, Tetrahedron Lett. 59 (2018) 592–604, https://doi.org/10.1016/j.tetlet.2018.01.004.
[52] J.L. Segura, R. Juárez, M. Ramos, C. Seoane, Hexaazatriphenylene (HAT) derivatives: from synthesis to molecular design, self-organization and device applications, Chem. Soc. Rev. 44 (2015) 6850–6885, https://doi.org/10.1039/C5CS00181A.
[53] H. Zhao, Y. Wang, R. Liu, W. Chen, Y. Wu, H. Cao, F. Lian, Preparation and electrochemical properties of porous organic polymer with high ionic diffusion coefficient as cathode material for lithium-ion batteries, J. Power Sources 626 (2025) 235733, https://doi.org/10.1016/j.jpowsour.2024.235733.
[54] L. Xu, L. Zhenhu, Y. Zhang, H. Guo, M. Zou, H. Li, Y. Liu, S. Liu, Stable hexaazatrinaphthylene-based covalent organic framework as high-capacity electrodes for aqueous hybrid supercapacitors, Energy Mater. 5 (2025) 500036, https://doi.org/10.20517/energymater.2024.127.
[55] P.N. Singh, M.G. Mohamed, M.G. Kotp, T. Mondal, S.V. Chaganti, M. Ibrahim, S. U. Sharma, Y. Ye, S.W. Kuo, Nitrogen- and sulfur-rich microporous carbons derived from conjugated microporous polymers for CO_2 uptake, supercapacitor energy storage, and electrochemical hydrogen production, ACS Appl. Polym. Mater. 7 (2025) 3324–3336, https://doi.org/10.1021/acsapm.5c00012.
[56] M.G. Mohamed, M.G. Kotp, A.O. Mousa, Y.S. Li, S.W. Kuo, Construction of Fe- and N-doped microporous carbon from ferrocene-based conjugated microporous polymers for supercapacitive energy storage, ACS Appl Energy Mater 8 (2025) 2389–2402, https://doi.org/10.1021/acsaem.4c02968.
[57] Q. Yuan, C. Li, X. Guo, J. Zhao, Y. Zhang, B. Wang, Y. Dong, L. Liu, Electrochemical performance and storage mechanism study of conjugate donor–acceptor organic polymers as anode materials of lithium-ion battery, Energy Rep. 6 (2020) 2094–2105, https://doi.org/10.1016/j.egyr.2020.08.001.
[58] S. Punyasloka, K. Higashimine, N. Matsumi, Donor–acceptor-based conjugated polymeric active material with enhanced pseudocapacitive contribution for ultrafast charging of lithium-ion batteries, ACS Appl Energy Mater 7 (2024) 5379–5389, https://doi.org/10.1021/acsaem.4c00404.
[59] M.G. Mohamed, S.Y. Chang, M. Ejaz, M.M. Samy, A.O. Mousa, S.W. Kuo, Design and synthesis of bisulfone-linked two-dimensional conjugated microporous polymers for CO_2 adsorption and energy storage, Molecules 28 (2023) 3234, https://doi.org/10.3390/molecules28073234.
[60] J. Wang, C.S. Chen, Y. Zhang, Hexaazatrinaphthylene-based porous organic polymers as organic cathode materials for lithium-ion batteries, ACS Sustain. Chem. Eng. 6 (2018) 1772–1779, https://doi.org/10.1021/acssuschemeng.7b03165.
[61] P. Xu, S. Ouyang, Q. Bai, Q. Ma, Y. Zhu, A hexaazatriphenylene-based porous organic polymer for high performance supercapacitor, J. Polym. Sci. 62 (2024) 1647–1653, https://doi.org/10.1002/pol.20230256.
[62] Z. Chen, Y. Wang, Z. Ning, Q. Huang, J. Zhou, F. Yu, Conjugated microporous polymer/TiS_2 composite cathode for high-performance lithium-rechargeable batteries, ACS Appl. Polym. Mater. 6 (2024) 13110–13119, https://doi.org/10.1021/acsapm.4c02203.
[63] T. Zhou, Y. Yuan, L. Xiao, W. Ding, Y. Wang, L.P. Lv, Boosting of redox-active polyimide porous organic polymers with multi-walled carbon nanotubes towards pseudocapacitive energy storage, Nanomaterials 14 (2024) 1388, https://doi.org/10.3390/nano14171388.
[64] M. Ejaz, M.G. Mohamed, Y.T. Chen, K. Zhang, S.W. Kuo, Porous carbon materials augmented with heteroatoms derived from hyperbranched biobased benzoxazine resins for enhanced CO_2 adsorption and exceptional supercapacitor performance, J Energy Storage 78 (2024) 110166, https://doi.org/10.1016/j.est.2023.110166.
[65] M.M. Samy, M.G. Mohamed, A.F.M. EL-Mahdy, T.H. Mansoure, K.C.W. Wu, S. W. Kuo, High-performance supercapacitor electrodes prepared from dispersions of tetrabenzonaphthalene-based conjugated microporous polymers and carbon nanotubes, ACS Appl. Mater. Interfaces 13 (2021) 51906–51916, https://doi.org/10.1021/acsami.1c05720.
[66] P. De, J. Halder, C.C. Gowda, S. Kansal, S. Priya, S. Anshu, A. Chowdhury, D. Mandal, S. Biswas, B.K. Dubey, A. Chandra, Role of porosity and diffusion

coefficient in porous electrode used in supercapacitors–correlating theoretical and experimental studies, Electrochem. Sci. Adv. 3 (2023) e2100159, https://doi.org/10.1002/elsa.202100159.
[67] S. Ragul, E. Sujithkrishnan, P. Elumalai, Inherent heteroatom-enriched amorphous carbon as high-performance electrode for sodium-ion battery and sodium-ion ultracapacitor, Energy Fuel 36 (2022) 15221–15233, https://doi.org/10.1021/acs.energyfuels.2c03153.
[68] M.Y. Perdana, B.A. Johan, M. Abdallah, M.E. Hossain, Md.A. Aziz, T.N. Baroud, Q. A. Drmosh, Understanding the behavior of supercapacitor materials via electrochemical impedance spectroscopy: a review, Chem. Rec. 24 (2024) e202400007, https://doi.org/10.1002/tcr.202400007.
[69] K. Kannadasan, V. Sankar Devi, S. Archana, P. Thomas, P. Elumalai, Deconvolution of capacitive and diffusive charge/lithium storage in lyophilized $NiCO_2S_4$–$NiCO_2O_4$ composite for supercapattery and lithium-ion battery, New J. Chem. 47 (2023) 13963–13978, https://doi.org/10.1039/D3NJ01663C.
[70] V. Augustyn, J. Come, M.A. Lowe, J.W. Kim, P.L. Taberna, S.H. Tolbert, H. D. Abruña, P. Simon, B. Dunn, High-rate electrochemical energy storage through Li^+ intercalation pseudocapacitance, Nat. Mater. 12 (2013) 518–522, https://doi.org/10.1038/nmat3601.
[71] W. Pholauyphon, P. Charoen-amornkitt, T. Suzuki, S. Tsushima, Guidelines for supercapacitor electrochemical analysis: a comprehensive review of methodologies for finding charge storage mechanisms, J Energy Storage 98 (2024) 112833, https://doi.org/10.1016/j.est.2024.112833.
[72] E. Quattrocchi, T.H. Wan, A. Curcio, S. Pepe, M.B. Effat, F. Ciucci, A general model for the impedance of batteries and supercapacitors: the non-linear distribution of diffusion times, Electrochim. Acta 324 (2019) 134853, https://doi.org/10.1016/j.electacta.2019.134853.
[73] C. Bathula, I. Rabani, A. Kadam, H. Opoku, S.A. Patil, N.K. Shreshta, J.H. Hwang, Y.S. Seo, H.S. Kim, Sonochemically exfoliated polymer-carbon nanotube interface for high performance supercapacitors, J. Colloid Interface Sci. 606 (2022) 1792–1799, https://doi.org/10.1016/j.jcis.2021.08.136.
[74] Y. Wang, J. Zhao, Y. Xing, Y. Dong, Z. Wang, Y. Hasebe, R.H. Baughman, Covalent organic framework derived oxygen/sulfur-doped porous carbon for robust high-capacitance symmetric supercapacitors, Chem. Asian J. 20 (2025) e202400930, https://doi.org/10.1002/asia.202400930.
[75] F. Fu, D. Yang, W. Zhang, H. Wang, X. Qiu, Green self-assembly synthesis of porous lignin-derived carbon quasi-nanosheets for high-performance supercapacitors, Chem. Eng. J. 392 (2020) 123721, https://doi.org/10.1016/j.cej.2019.123721.
[76] T. Li, X. Yan, W.D. Zhang, W.K. Han, Y. Liu, Y. Li, H. Zhu, Z. Li, Z.G. Gu, A 2D donor–acceptor covalent organic framework with charge transfer for supercapacitors, Chem. Commun. 56 (2020) 14187–14190, https://doi.org/10.1039/D0CC04109B.